applied sciences

MDPI

Article

Feasibility of Conventional Non-Destructive Testing Methods in Detecting Embedded FRP Reinforcements

Pranit Malla [1,*], Seyed Saman Khedmatgozar Dolati [1], Jesus D. Ortiz [2], Armin B. Mehrabi [1,*], Antonio Nanni [2] and Kien Dinh [3]

[1] Department of Civil and Environmental Engineering, Florida International University, Miami, FL 33174, USA; skhed004@fiu.edu
[2] Department of Civil and Architectural Engineering, University of Miami, Coral Gables, FL 33146, USA; jdo72@miami.edu (J.D.O.); nanni@miami.edu (A.N.)
[3] NDT Concrete LLC, Deltona, FL 32725, USA; kien@ndt-concrete.com
* Correspondence: pmall011@fiu.edu (P.M.); amehrabi@fiu.edu (A.B.M.)

Abstract: Fiber-Reinforced Polymer (FRP) bars/strands are the most promising alternative to their steel counterparts for reinforcing concrete elements due to their resistance to corrosion, lighter weight, higher strength and better durability. However, very limited research has been conducted in relation to non-destructive testing (NDT) methods that are applicable to damage detection in FRP bars or the detection of FRP reinforcements embedded in concrete. The ability to assess the condition of the relatively new and unique FRP reinforcements will increase the confidence of the construction industry in their use as a reliable substitute for steel reinforcements. This paper investigates the ability of two of the most commonly used NDT methods, Ground Penetrating Radar (GPR) and Phased Array Ultrasonic (PAU), in detecting FRP bars/strands embedded in concrete elements. GPR and PAU tests were performed on two slab specimens reinforced with GFRP (Glass-FRP) bars, the most commonly used FRP bar, with variations in their depth, size and configuration, and a slab specimen with different types of available FRP reinforcements. The results show that GPR devices can detect GFRP bars/strands and CFRP (Carbon-FRP) strands to some extent, and their detectability increases with the increase in their antenna center frequency. On the contrary, PAU is only capable of detecting GFRP and CFRP strands. The results of this paper also emphasize the need for further research and developments related to NDT applications to embedded FRP bars.

Keywords: fiber-reinforced polymer (FRP); ground penetrating radar (GPR); ultrasonic testing (UT); phased array ultrasonic (PAU); non-destructive testing (NDT); reinforced concrete

check for updates

Citation: Malla, P.; Khedmatgozar Dolati, S.S.; Ortiz, J.D.; Mehrabi, A.B.; Nanni, A.; Dinh, K. Feasibility of Conventional Non-Destructive Testing Methods in Detecting Embedded FRP Reinforcements. *Appl. Sci.* **2023**, *13*, 4399. https://doi.org/10.3390/app13074399

Academic Editor: Michel Darmon

Received: 2 March 2023
Revised: 28 March 2023
Accepted: 29 March 2023
Published: 30 March 2023

Copyright: © 2023 by the authors. Licensee MDPI, Basel, Switzerland. This article is an open access article distributed under the terms and conditions of the Creative Commons Attribution (CC BY) license (https://creativecommons.org/licenses/by/4.0/).

1. Introduction

Corrosion of steel reinforcement is one of the main problems in traditional concrete structures, which severely affect its safety and serviceability. Several corrosion protection measures, including but not limited to cathodic protection, epoxy-coated bars and galvanized steel reinforcements have been implemented in the past; however, they have only managed to delay corrosion rather than eradicating it [1]. The most promising alternatives available that could entirely stop the process of corrosion within concrete is the use of fiber-reinforced polymer (FRP) bars/strands [2–6]. Depending upon the types of reinforcing fibers used, the FRP bars/strands can be classified as GFRP (Glass-FRP), CFPR (Carbon-FRP), BFRP (Basalt-FRP) and AFRP (Aramid-FRP) bars, respectively for glass, carbon, basalt and aramid fibers. The FRP bars are resistant to all the elements that leads to corrosion in steel reinforced concrete (RC) structures, such as reduction of pH of the concrete from carbonation, chloride contamination of the concrete and diffusion of halides and chemicals [7,8]. The use of FRP bars for reinforcing new structures is even more preferable because they also have 1.5–2 times higher tensile strength than their steel counterparts [9–11]. In addition, although the initial cost of FRP bars is higher than that

of the conventional steel bars, their life cycle cost analysis indicates that it can be quite economical in the long term [12]. Given these circumstances, the embedded FRP bar is gradually becoming a trusted material in civil engineering.

To ensure construction quality and continued structural reliability, the necessity for innovative non-destructive testing (NDT) methods or research on the feasibility of existing NDTs becomes more apparent with the rise in use of unique structural materials such as FRP bars. Although higher durability and performance are associated with the FRP bars in some respects when compared to steel, concerns still remain regarding damages and defects in this material, many of them rather unique, such as debonding, delamination and aging from UV exposure. It is equally important to understand the damages and defects associated with the use of FRP bars as it is for other structural materials. Further, it is even more crucial to identify the signs of possible failure of structures reinforced with FRP bars at the earliest because they are not as ductile as conventional constructions [13] and do not display any exterior warnings of damage until they break [14].

However, there has only been minimal or non-existing work carried out for assessment of FRP embedded within concrete. The only available comprehensive guide for the inspection of FRP application in civil engineering is the NCHRP report 564 [15], which is limited to the inspection of FRP bridge decks. Currently, there is no guide or manual for the inspection of FRP-reinforced concrete elements [16,17]. This is in most part because of the lack of research on non-destructive testing and inspection of such elements. Most FRP bars are undetectable or have low detectability and therefore cannot be effectively located in the inspection, which makes detection of their damages difficult. The use of FRP material in highway construction has increased consistently [18–21], but the lack of methods for condition assessment of FRP-RC has noticeably dampened the proliferation of FRP use. Bridge owners are not comfortable with products that cannot be detected properly and whose condition cannot be effectively assessed for maintenance purposes. Hence, there is a strong need for research on the means and methods of condition assessment of FRP-RC, the availability of which will have exponential effects in increasing the use of FRP in future constructions. The main objective of this paper is to determine the feasibility of the most common NDT methods in detecting embedded FRP bars/strands, which would act as an initial step for propelling future studies on the nondestructive testing of FRP bars/strands.

Many NDT techniques, such as visual inspection (VT) [9,22], tap testing (TT) [23–27], impact echo testing (IE) [28–32], microwave testing (MW) [33–38], ground penetrating radar (GPR) [39–47], ultrasonic testing (UT) or phased array ultrasonic testing (PAU) [48–55], infrared thermography testing (IR) [56–64], acoustic emission testing (AE) [65–68], laser testing (LT) [69–75], radiographic testing (RT) [76–81], global structural response testing [82–87], etc., have been studied for detecting damages in the externally applied FRP composites. However, the inspection of FRP-reinforced concrete members are limited to detection of debonding between internal FRP bars and concrete [88,89] or initiation of breakage in FRP [14,90] rather than the detection of the bars themselves. Hence, among several available NDTs, this paper aims to determine the feasibility of using commercially available GPR and PAU for detecting embedded FRP bars in concrete as they are the most common methods in the NDT practice for steel RC elements [16,91,92]. In 2019, Drobiec et al. confirmed that GPR and PAU have limited detectability of non-metallic reinforcement (FRP reinforcements), but they had only conducted tests on the fiber meshes of FRPs [93]. However, this paper will further explore the potential of these devices in detecting the FRP bars and strands used in FRP-reinforced concrete. The results of this study show that lower frequency GPR devices are able to detect larger FRP bars/strands at shallower depths with improvements in their detectability with the use of higher antenna center frequency devices. The results also indicate that PAU devices are only effective for detecting GFRP and CFRP prestressing strands.

2. Materials and Methods

In order to determine whether GPR and PAU can detect internal FRP reinforcement, small-scale concrete slabs were fabricated. Two slab specimens (i.e., labeled as J and L) were 30 in. wide by 30 in. long and 7 in. deep, and the third specimen (viz. Slab C) was 36 in. wide by 36 in. long and 5 in. deep. The concrete mix used to cast the slab specimens was the 'Class II 4500 Bridgedeck' concrete, as per the Florida Department of Transportation (FDOT). This class specified a guaranteed compressive strength of 4600 psi (31 MPa). Type II Cement was used with a water to cementitious material ratio (w/m) of 0.44, and #57 stone and silica sand was used as coarse and fine aggregate, respectively. To obtain the actual strength value; concrete cylinders were tested at 28 days according to ASTM C39 [94,95]. An average compressive strength of 31.70 MPa was obtained with a standard deviation of 0.69 MPa (coefficient of variation of 2.2%).

The slab specimens were fabricated, targeting different parameters such as FRP bars/strands type (GFRP, CFRP, BFRP), bar diameter, bar direction and bar depths. Table 1 shows the identification of the slab specimens by group, highlighting their main parameters. Because GFRP bars are the most commonly used FRP reinforcement in concrete elements, the first two slabs constructed (Slabs C and J) were only reinforced with GFRP bars of different sizes, at different depths and different configuration (bars in one direction and bars in two orthogonal directions, i.e., mesh). The concrete cover specified by ACI CODE-440.11-22 [96] for the concrete members reinforced with GFPR bars ranges from 0.75 in. to 3 in., hence the depth variations in the slab specimens were included to represent the layers of FRP reinforcement, which could be anywhere within the concrete cover range specified. Further, the third slab (Slab L) has different types of internal reinforcement (bars and strands) embedded into it, including one steel bar whose detectability acts as a control for this research. Having GFRP, CFRP, BFRP and steel bars/strands on the same slab specimen allows comparison of the detectability of different FRP bar/stands with the steel bar under the same test conditions.

Table 1. Identification of small-scale concrete slab specimens.

Specimen Group	Slab ID	Bar Diameter	No. of Bars
Slabs with GFRP bars in one direction	Slab C	#4 and #6	6
Slabs with GFRP bars in two directions (mesh)	Slab J	#6	10
Slab with different FRP bars in one direction	Slab L	#3, #5, #8 GFRP bars, #5 CFRP strand, #3 steel bar, #6 GFRP strand, #3, #5 BFRP bars	9

All specimens were fabricated and labeled following the same layout as shown in Figure 1. Every slab is identified with a letter (C, J and L), and every side has an identification number (from 1 to 4). The direction of the measurement will be determined by the number where the measurement is started to the end of the measurement.

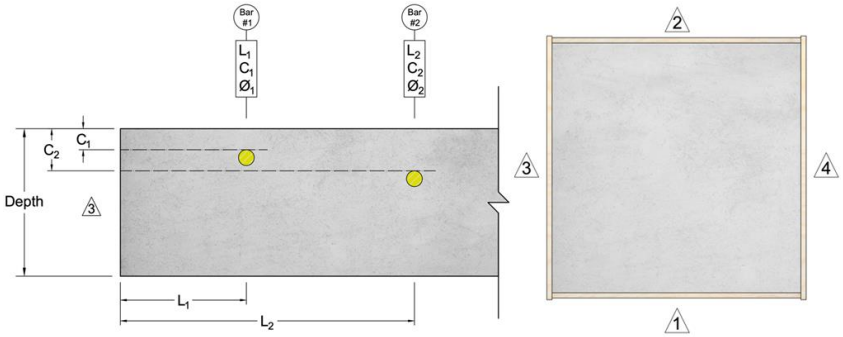

Figure 1. Labeling of slab specimens.

Table 2 shows the details and dimensions of the specimens. For each specimen, the distance to edge, depth to surface, bar diameter, bar material and slab depth are presented based on the convention shown in Figure 1. The formwork for each slab specimen constructed is shown in Figure 2.

Table 2. Reinforcement/Dimension details of detectability slab specimens.

Slab ID	Parameter [Symbol/Units]	Reference Side	Bar 1	Bar 2	Bar 3	Bar 4	Bar 5	Bar 6	Bar 7	Bar 8	Bar 9	Bar 10
C	Distance to edge reference (L/in.)	3	3	9	15	21	27	33				
	Depth to surface (C/in.)		0.75	0.75	1.5	1.5	3	3				
	Diameter of bar (F/in.)		#4	#6	#4	#6	#4	#6				
	Material of bar (T)		Glass									
	Depth of slab (h/in.)		5.0									
J	Distance to edge reference (L/in.)	3	3.3	8.6	14.5	20.2	25.4	(Bottom mesh)				
	Depth to surface (C/in.)		3.3	3.3	3.6	3.5	3.8					
	Diameter of bar (F/in.)		#6									
	Material of bar (T)		Glass									
	Depth of slab (h/in.)		7.0									
	Distance to edge reference (L/in.)	1	(Top Mesh)					3.3	8.6	14.5	20.2	25.4
	Depth to surface (C/in.)							2.6	2.6	2.9	2.8	3.1
	Diameter of bar (F/in.)							#6				
	Material of bar (T)							Glass				
	Depth of slab (h/in.]							7.0				
L	Distance to edge reference (L/in.)	3	4.3	7.1	10.3	13.1	16.4	18.8	21.6	24.8	27.6	
	Depth to surface (C/in.)		4.2	3.3	3.6	3.9	3.9	4.0	3.8	4.1	4.0	
	Diameter of bar (F/in.)		#3	#8	#5	#5	#5	#3	#6	#3	#5	
	Material of bar (T)		Glass				C-Std *	Steel	G-Std *	Basalt		
	Depth of slab (h/in.)		7.0									

* C-Std. (i.e., CFRP strands) and G-Std (i.e., GFRP strands) are labelled as Bar 5 and Bar 7 in Slab L.

2.1. GPR Tests

Ground penetrating radar (GPR) is a non-destructive testing (NDT) method that is used to the analyze internal characteristics of structures or elements in real-time. It works on the principle that electromagnetic waves reflect back when they encounter an interface between two materials with different dielectric constants [31,39]. GPR functions by emitting electromagnetic waves (in the form of radio waves) through the test material and then detecting the waves that bounce back off any discontinuities within the material. These discontinuities can take various forms, including interfaces between different materials, such as the concrete-bar interface shown in Figure 3 or the concrete-air/water interfaces (subsurface defects like voids, cracks, debonding and delamination) [97]. Due to the limited research on the use of GPR for FRP-reinforced structures, this method has not yet been able to establish itself as a reliable NDT method. This paper will explore the possibility of using GPR for FRP bar detection.

In this study, the GPR tests were conducted both as individual line scans along a straight line and as grid scans over a test area. The line scans were conducted as a reconnaissance survey or preliminary inspection prior to the detailed grid/area scan to form a quick idea of what to expect inside the structure, the orientation of reinforcement or other subsurface features, and the depth of exploration. The GPR line scans conducted

along a straight line on the surface of the test specimen were used to obtain its cross-section image through a plane normal to the surface along the direction of the scan. However, going back and forth between several line scans and interpretating each line scan was time consuming and labor intensive. Thus, in order to simplify the interpretation of results, grid scans were also conducted over the surface of the test specimens. Grid scans were performed simply by taking GPR data along the straight lines of a grid over an area covering the test specimen, as shown in Figure 4. The grid required for a grid scan was arranged using a grid mat secured to the surface so that it did not move while taking the GPR data.

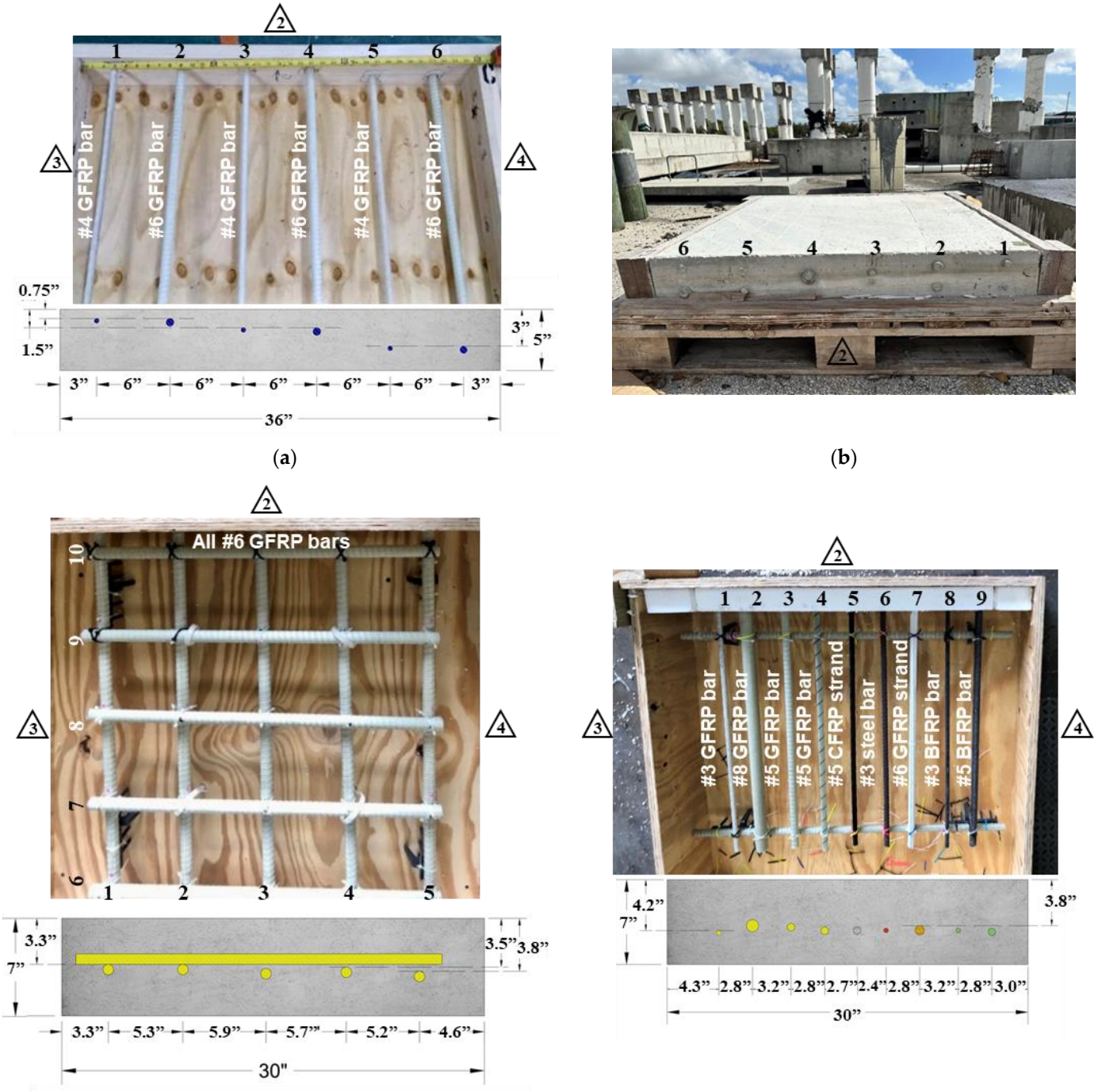

Figure 2. FRP bars in different slabs: (**a**,**b**) Slab C, (**c**) Slab J, (**d**) Slab L.

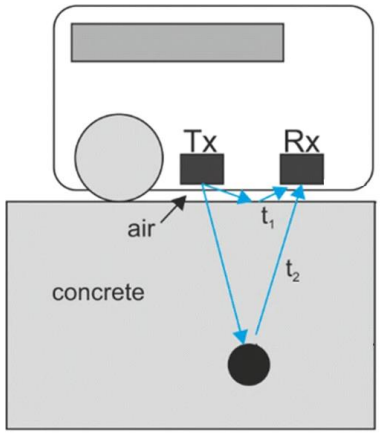

Figure 3. Reflection of incident wave at concrete–bar interface [98].

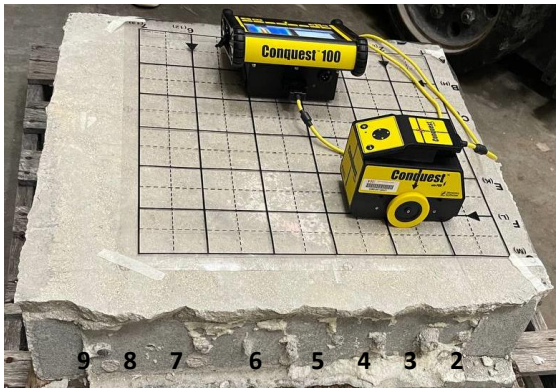

Figure 4. GPR grid scan test setup for Slab L.

The spacing between each scan in the grid were set as 2 in. for this study. The spacing between the individual lines in the grid determines the resolution of the data collected and it is termed as grid resolution. The lower the spacing between each line scans in a grid, the higher the resolution of the data collected. Hence, the images will be clearer, and it would be easier to interpret the data. Apart from using closely spaced grid lines, a higher GPR frequency can also be used to increase the resolution. The depth of penetration and the resolution of a GPR depends upon the frequency of the pulse transmitted into the material. Lower frequencies allow deeper penetration with lower resolution, whereas higher frequencies allow detection of small defects (higher resolution) but localized within a shallower depth [31,93,99,100]. Four different GPR systems with different center frequency ranges were used in this experiment to determine the effect of GPR frequency on the bar detectability, as shown in Table 3 and Figure 5. The data acquired from grid scans were used to give the cross-section image of the test specimen through the plane parallel to the surface of the specimen along its depth. The cross-sectional image along the depth of the specimen is termed as a depth slice or time slice image.

Table 3. Technical specifications of the GPR systems used [101–104].

GPR Systems	Center Frequency	Radar Technology	Depth Range	Manufacturer
Conquest 100 Enhanced	1000 MHz	Monostatic GPR antenna	24 in. (60 cm)	Sensors and Software, Canada
C-Thrue radar	2000 MHz	Dual polarization antenna for multi-level detection	31.5 in. (80 cm)	IDS GeoRadar, Italy

Table 3. *Cont.*

GPR Systems	Center Frequency	Radar Technology	Depth Range	Manufacturer
Proceq GP8800	400–6000 MHz	Stepped-frequency continuous-wave (SFCW) GPR	25.6 in. (65 cm)	Screening Eagle Technologies, Switzerland
Proceq GP8000	200–4000 MHz	Stepped-frequency continuous-wave (SFCW) GPR	31.5 in. (80 cm)	Screening Eagle Technologies, Switzerland

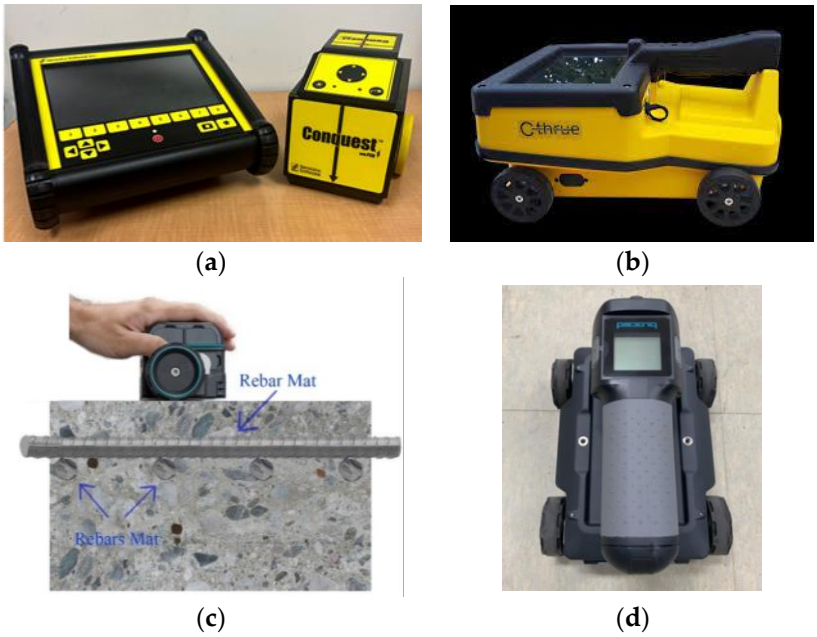

Figure 5. GPR systems used: (**a**) Conquest 100 Enhanced, (**b**) C-Thrue radar [105], (**c**) Proceq GP8800 [106], (**d**) Proceq GP8000 [107].

2.2. PAU Tests

Ultrasonic testing (UT) operates on the principle that the incident ultrasonic waves generated by ultrasonic transducers (which transform electrical or optical signals into ultrasonic waves and vice versa) will be reflected back when they encounter an interface between two materials with different acoustic impedances. A phased array ultrasonic (PAU) is an advancement over the UT technology that can be achieved when several of these transducers are arranged together into an array and operated at slightly different times (either electrically or physically) so that the individual waves interact both positively and negatively, allowing beam focusing and beam steering, as shown in Figure 6 [108]. The advantages of PAU in comparison to conventional UT include a 5 to 10 times faster scanning rate, better images due to multiple angles and frequencies, which require less interpretation, higher resolution, capability of beam focusing, reliability, portability and mobility [109,110]. Unlike conventional UT, PAU testing allows signal focusing at desired locations and angles, which is advantageous for the testing of composite materials that have an anisotropic structure, creating challenges in signal evaluation [53,111]. However, PAU is a relatively new technique compared to the traditional NDTs, and hence the limitations of portable units of PAU include the uncertainty in its application as it has yet to be completely proven.

Line scan using PAU was performed by moving the array of ultrasonic transducers in a sideways direction along the desired line of inspection, as shown in Figure 7. Each scan at individual positions is stitched together to give one continuous line scan, which is the cross-sectional image through a plane normal to the surface along the direction of the scan. Similarly, the area scan using PAU was conducted as a stripe scan. The stripe scan was performed by positioning the array of ultrasonic transducers perpendicular to the desired line of inspection and then taking scans while moving forward with desired spacing

between the consecutive scans, as shown in Figure 7. Each individual scan collected during stripe scan is simply a line scan having a width of measurement equal to that of the PAU device or the array of transducers. These individual scans along the line of inspection are stitched together to give a time slice or depth slice view, which can be further processed into a full 3D iso-surface representation. The depth slice view is simply the cross-section image parallel to the surface scanned.

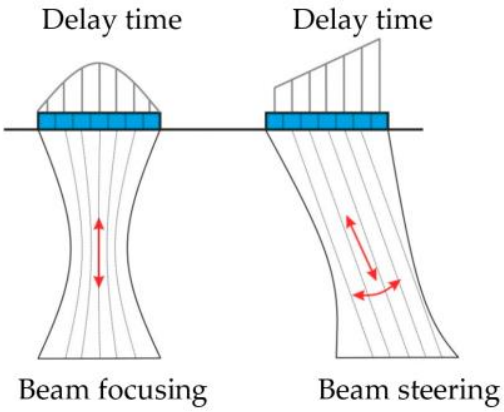

Figure 6. Phased array with angled wavefront [112].

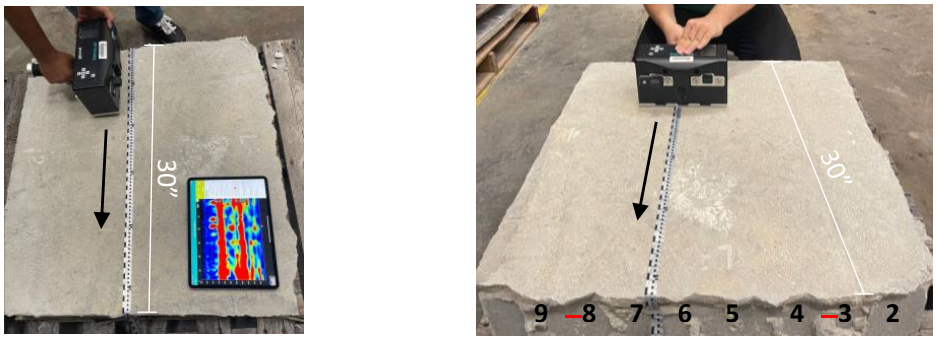

(**a**) (**b**)

Figure 7. PAU test setup: (**a**) Line scan, (**b**) Stripe scan.

Two different PAU systems were used in this experiment to determine their FRP bar detection capability, as shown in Table 4 and Figure 8. The MIRA 3D device had 64 ultrasonic transducers located in a 16 × 4 grid at 3 cm spacing (extended 16 rows of 4 transducers each) where the Pundit Live Array Pro had 24 ultrasonic transducers located in an 8 × 3 grid at 3 cm spacing (8 rows of 3 transducers each).

(**a**) (**b**)

Figure 8. PAU systems used: (**a**) A1040 MIRA 3D (two devices were attached side by side to increase the number of channels to 16 rows of 4 transducers each) [115], (**b**) Pundit live array pro.

Table 4. Technical specifications of the PAU systems used [113–115].

PAU Systems	Number of Channels	Technology	Transducer	Bandwidth	Depth Range	Manufacturer
A1040 MIRA 3D	8 × 4 (extendable to 16 × 4, 24 × 4, etc.)	Multi-channel ultrasonic pulse echo tomograph	Active dry point contact (A-DPC) transducers	10–100 KHz	6.5 ft (2 m)	ACS-Solutions GmbH, Germany
Pundit live array pro	8 × 3 (with upgrade option to 16 × 3)	Phased array ultrasonic pulse echo	Dry-contact Pundit Array transducer	15–100 KHz	6.6 ft (2 m)	Screening Eagle Technologies, Switzerland

3. Results

3.1. GPR Tests Results

GPR response or line views traversing perpendicular to bars embedded in each slab specimens obtained using a 1 GHz GPR device are shown in Figure 9, where the top of the hyperbolic shape, i.e., inverted U shape, indicates the location of the bar and the shape of the tails gives a measure of velocity and depth [116]. The background subtraction filter was used to enhance the hyperbolas from embedded FRP bars. Without the application of this filter, the top of the hyperbola of the shallow targets (FRP bars close to the top surface) would have been obscured by the direct wave band that appears at the top surface. However, using the filter also removed the horizontal band indicating the bottom surface of the slab, but because the main objective of this research was to detect the FRP bars, the detection of the bottom surface was deemed not important. Only the line scans conducted at the centerline of the slabs using the lowest frequency GPR device has been presented in this paper for the brevity of the results as it would represent the lowest resolution among the GPR devices used in this study. Further, it should be noted that in order to confirm that the hyperbolas detected were indeed the FRP bars, but not other internal features (such as voids), several line scans were performed and checked for repetition of the same pattern of hyperbolas in each line scan (which indicates the presence of a continuous internal target such as a reinforcement bar). For Slab C with GFRP bars in one direction, bars at up to a depth of 1.5 inch were detectable. For Slab J with GFRP bars in two directions (mesh), the hyperbolas for the bars on both the top and bottom mesh were detectable. The bars near the edge were shadowed by the hyperbola due to the edge of the slab, which could have been avoided by leaving an offset from the edge for taking the measurements. The GPR line scan of Slab L was able to detect carbon strand (Bar 5), steel bar (Bar 6) and GFRP strand (Bar 7), along with the larger diameter #8 GFRP bar (Bar 2). However, it was not able to detect other glass (Bars 1, 3, 4) and basalt (Bars 8, 9) bars. The bar detectability of the line scans conducted using lower frequency device is further summarized in Table 5.

Table 5. Bar detectability in line scans performed using Conquest 100 Enhanced.

Slab ID	Bar 1	Bar 2	Bar 3	Bar 4	Bar 5	Bar 6	Bar 7	Bar 8	Bar 9	Bar 10
C	✓	✓	✓	✓	X	X	-	-	-	-
J	✓	✓	✓	✓	✓	X	✓	✓	✓	✓
L	X	✓	X	X	✓	✓	✓	X	X	-

Note: ✓ = detectable, X = not detectable.

The depth slices obtained for each slab specimen using each GPR device are further illustrated in Figure 10, where it can be seen that the bar detectability improves as the device central frequency increases. Although the line scan in Figure 9a shows four hyperbolas for Bars 1–4, the depth slice in Figure 10a only shows the presence of Bar 2, which is the larger GFRP bar (#6 GFRP bar) at shallower depth in Slab C. This could be because of the limitations in vertical resolution due to a lower frequency of the GPR device. Larger GFRP bars are detectable using lower frequency GPR device at shallower depth, but they return weaker hyperbolas in comparison to metallic objects. Moreover, the relatively higher

amplitude of shallower GFRP bars may have dominated and masked the lower amplitude returns from the GFRP bar that are deeper and smaller in diameter, which could be the reason only Bar 2 was visible in Figure 10a. However, the depth slices in Figure 10b,c, obtained using higher frequency GPR devices, are capable of detecting a smaller diameter bar, even at deeper depths.

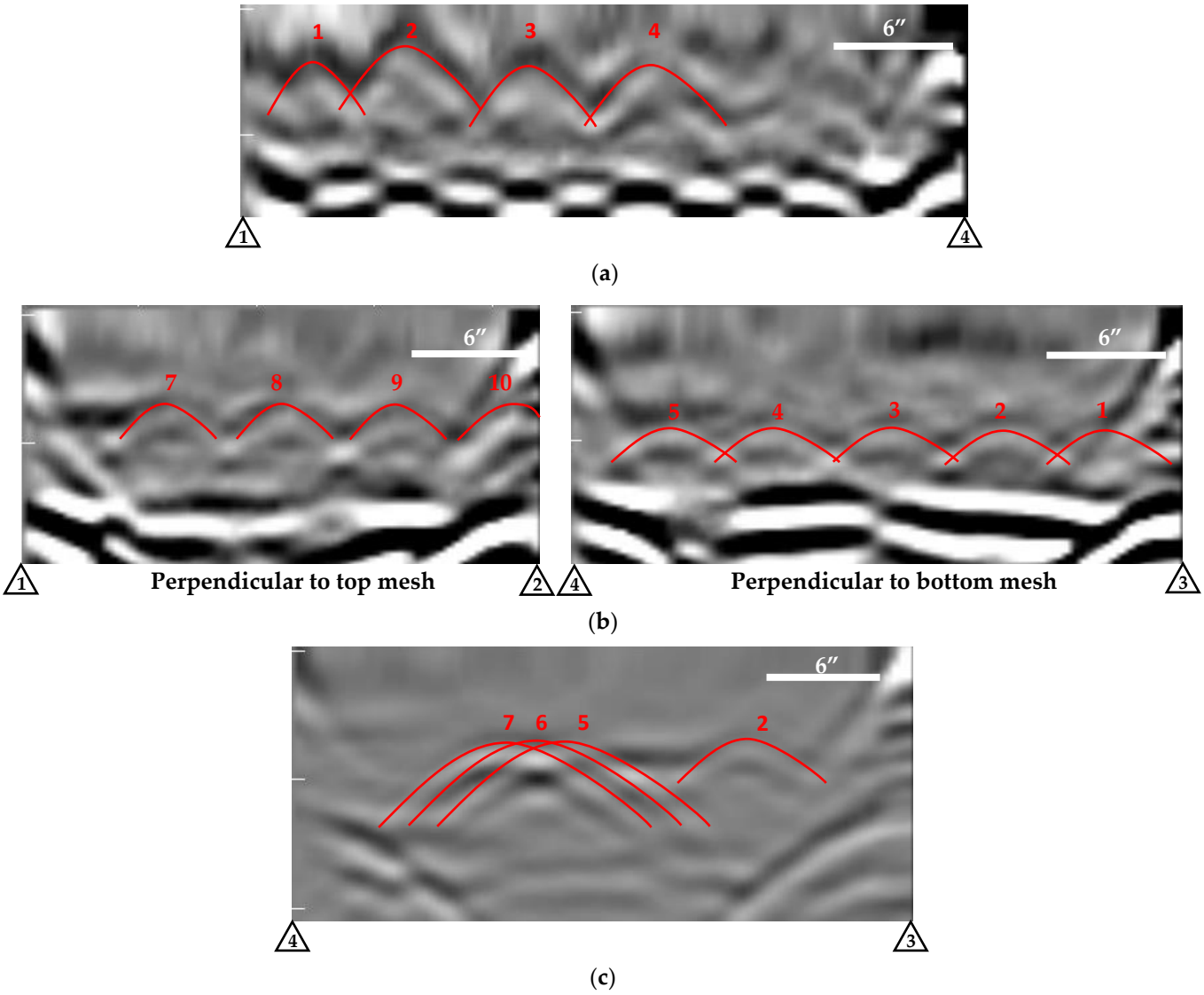

Figure 9. Line scan results of Conquest 100 Enhanced for different slab specimens: (**a**) Slab C, (**b**) Slab J, (**c**) Slab L.

In the case of depth slices for Slab J with a top and bottom mesh of GFRP bars, all the GPR devices could clearly detect the top mesh of #6 GFRP bars at a shallower depth, while the bottom mesh was only visible for the higher frequency GPRs, as shown in Figure 10d–f. The inability of lower frequency GPR to show the bottom mesh could be due to the same reason for not showing deeper GFRP bars in Slab C, as explained previously. In addition to the higher center frequency of the 2 GHz GPR device, its dual polarization feature further permits detection on both first and second levels of bars, whereas for the GPR device with maximum center frequency of 4 GHz and 6 GHz, the ability to detect the bottom mesh is solely due to the higher resolution, which it can afford because of its higher frequency.

The line scan of Slab L shows that Bar 2 (#8 GFRP bar) is visible as a faded hyperbola in addition to distinctive hyperbolas of Bars 5, 6 and 7. But again, Bar 2 is not visible in the depth slice in Figure 10g because GFRP bars return weaker hyperbolas in comparison to

steel bars (Bar 6) and the high amplitude steel bar dominates and hides the lower amplitude returns from the GFRP bar. In Figure 10g–i, it can be seen that the strongest detection is that of the steel bar (Bar 6), followed by the carbon strand (Bar 5) and GFRP strand (Bar 7). Carbon strands, in addition to having cavities from the twisting shape of exterior wires that are filled (or not filled) with concrete, they are also electrically conductive, which could be the reason they are distinctively visible, and the GFRP strands are visible only because of the cavities within the GFRP twisting wires. Apart from Bars 2, 5, 6 and 7, the higher frequency GPR was also able to capture other bars, as shown in Figure 10i.

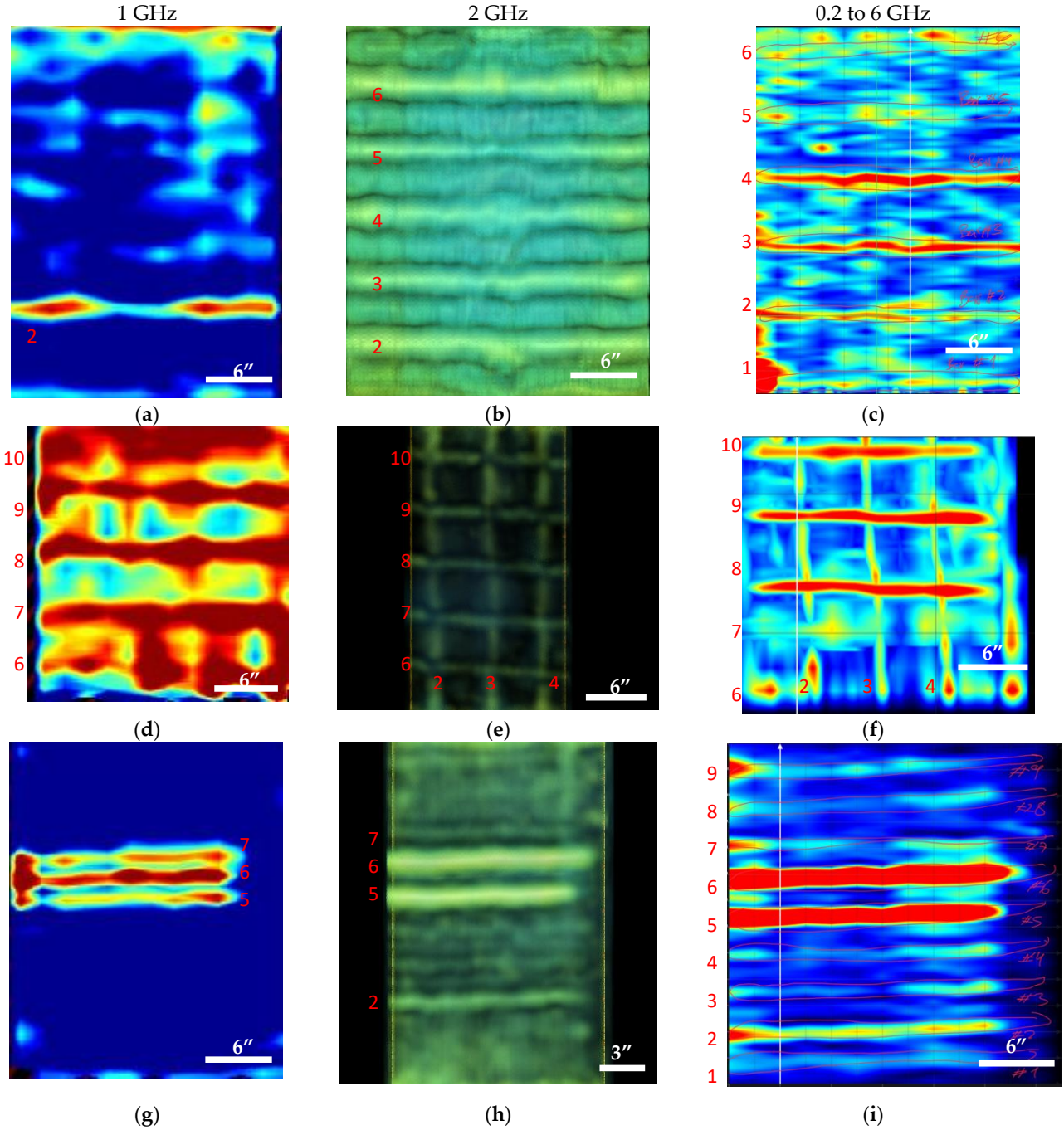

Figure 10. Depth slices: (**a**) Slab C using Conquest 100 Enhanced, (**b**) Slab C using C-Thrue, (**c**) Slab C using Proceq GP8800, (**d**) Slab J using Conquest 100 Enhanced, (**e**) Slab J using C-Thrue, (**f**) Slab J using Proceq GP8800, (**g**) Slab L using Conquest 100 Enhanced, (**h**) Slab L using C-Thrue, (**i**) Slab L using Proceq GP8000.

3.2. PAU Tests Results

The results of line scans and the area scans obtained from the PAU testing on each slab specimen using MIRA 3D and Pundit Live Array Pro devices are shown in Figure 11. It can be seen that PAU could not detect bars in Slab C and Slab J. However, it was able to detect carbon strands, steel bars and GFRP strands in Slab L. As ultrasonic testing and PAU is very sensitive in detecting the presence of (air) voids, their ability for detecting CFRP and GFRP strands could be attributed to the presence of (air) voids within the twisted FRP cables of these strands.

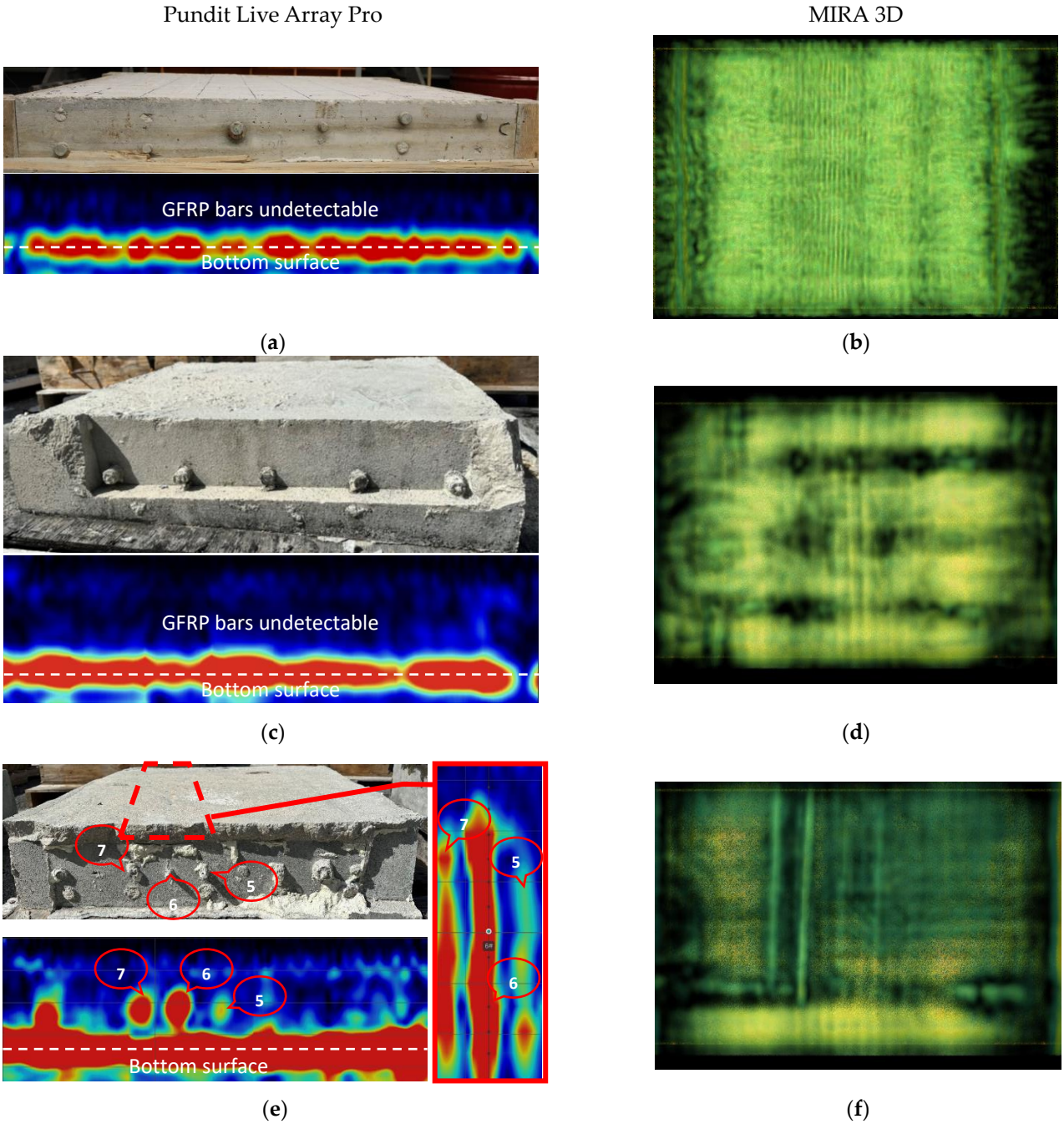

Figure 11. PAU test results: (**a**) Slab C line scan using Pundit, (**b**) Slab C area scan using MIRA 3D, (**c**) Slab J line scan using Pundit, (**d**) Slab J area scan using MIRA 3D, (**e**) Slab L line scan and stripe scan using Pundit, (**f**) Slab L area scan using MIRA 3D.

4. Discussion

The GFRP bars that dominate the embedded concrete reinforcement application are not conductive and have a density similar to concrete. Therefore, the conventional NDT methods that use electromagnetic and stress waves for the detection of steel bars fail to detect GFRP bars with the same clarity as steel. As explained earlier in Sections 2.1 and 2.2, the GPR and PAU devices work on the basis of differences in dielectric constant and acoustic impedance encountered at an interface. The reflection coefficient of the electromagnetic wave (for GPR tests) and ultrasonic waves (for PAU tests) passing through concrete when they encounter air (bottom surface), steel bar and GFRP bars are shown in Table 6. It can be seen that the concrete–GFRP interface reflection coefficient, i.e., the amount of reflected energy, is less than 8% for GPR tests and has a very minimal value of 0.04% for PAU tests, which is the reason why GPR had limited detectability of GFRP bars and PAU was not able to detect them at all. The dielectric constants and acoustic impedances for average concrete, air and steel used in Table 6 were obtained from the literature [116–118]. From the specifications chart provided by the manufacturer of the GFRP bar, the dielectric constant was determined to be a value of less than 5, and the acoustic impedance was estimated to be 10.7 $\times$ 10^6 kg/m^2 s (from the equation $Z = \sqrt{E.\rho}$, where E = 54.5 GPa is the modulus of elasticity and ρ = 2.1 g/cm^3 is the density of the GFRP bar).

Table 6. Reflection coefficients for GPR and PAU tests.

Interface	Relative Dielectric Constant or Permittivity, ε		GPR Reflection Coefficient, R	Acoustic Impedance (10^6 kg/m^2 s), Z		PAU Reflection Coefficient, R
	ε_1	ε_2	$\frac{\sqrt{\varepsilon_1}-\sqrt{\varepsilon_2}}{\sqrt{\varepsilon_1}+\sqrt{\varepsilon_2}}$	Z_1	Z_2	$\frac{(Z_2-Z_1)^2}{(Z_2+Z_1)^2}$
Concrete-Air	7	1	45%	9.6	0.000429	99%
Concrete-Steel	7	∞	100%	9.6	46.5	43%
Concrete-GFRP	7	<5	<8%	9.6	10.7	0.30%

However, the depth slices of GPR tests obtained using four different devices with different antenna center frequency demonstrated that the detection of FRP bars becomes better with the increase in frequency, as shown in Table 7. Apart from the frequencies playing the major role in the detection of FRP bars, different detectability levels could also be due to several other factors related to the radar technologies being used in each of the GPR devices. For example, the 2 GHz GPR device also had a dual polarization feature that enhances the detection of multilevel bars. The maximum frequency GPR devices used in this study also had a Stepped Frequency Continuous Wave (SFCW) system. This provides both the benefits of higher resolution in the detection of shallow targets and the increase in penetration depth. Moreover, there were some disparities in the results of the line scans and the grid scans for the lower frequency GPR device as the bars visible in the line scan were not visible in the depth slices. This could be due to the fact that the depth slices are produced through the interpolation of a series of line scans, and it would show the bars with stronger signals, i.e., stronger hyperbola more dominantly in comparison to the bars with relatively weaker hyperbola. Thus, although it is time consuming, it is recommended to go through each line scan of a grid while analyzing the results for GPR tests. On the other hand, it was found that PAU can only detect FRP strands, which could be due to the presence of (air) voids within the twisted wires of FRP or irregularity of the shape of their surface in comparison with smooth bars.

Table 7. Bar detectability in depth slices performed using devices with different center frequency.

Slab ID	Center Frequency	Bar 1	Bar 2	Bar 3	Bar 4	Bar 5	Bar 6	Bar 7	Bar 8	Bar 9	Bar 10
C	1 GHz	X	✓	X	X	X	X	-	-	-	-
	2 GHz	✓	✓	✓	✓	✓	✓	-	-	-	-
	0.2 to 6 GHz	✓	✓	✓	✓	✓	✓	-	-	-	-
J	1 GHz	✓	✓	✓	✓	✓	X	X	X	X	X
	2 GHz	✓	✓	✓	✓	✓	✓	✓	✓	✓	✓
	0.2 to 6 GHz	✓	✓	✓	✓	✓	✓	✓	✓	✓	✓
L	1 GHz	X	X	X	X	✓	✓	✓	X	X	-
	2 GHz	X	✓	X	X	✓	✓	✓	X	X	-
	0.2 to 6 GHz	✓	✓	✓	✓	✓	✓	✓	✓	✓	-

Note: ✓ = detectable, X = not detectable.

5. Summary and Conclusions

The objective of this research was to determine the feasibility of using commercially available NDT methods such as GPR and PAU in detecting FRP bars embedded in concrete. These two NDT methods were tested over several parameters, such as FRP type, bar diameter, bar direction, and bar depths to determine their limitations and detection capabilities. Detecting the FRP bars embedded in concrete is the first obstacle to be overcome before being able to detect damages for ensuring their structural safety. Thus, the long-term objective of this study is to promote the research on NDT methods applicable to embedded FRP bars, which could help in proliferating their use in the construction industry.

In conclusion, the results of this study show that NDT methods that rely on electromagnetic waves such as Ground Penetrating Radar (GPR) become less effective, if not obsolete for non-metallic/non-conductive embedded bars. However, with the increase in center frequency of the GPR device, the detectability of FRP bars can be fairly improved. Similarly, other NDT methods such as Ultrasonic Testing (UT) or Phased Array Ultrasonic (PAU) that are based on stress waves have some capability for detecting steel reinforcement, but they perform poorly for the detection of the most commonly used FRP embedded bars (GFRP bars) but are good for detecting FRP strands.

However, there are some limitations related to the research conducted in this paper, which can be further explored and incorporated in the future studies related to NDT methods for the inspection of FRP-reinforced concrete elements. The scope of this study was limited to the real time test results obtained from post processing tools embedded within the devices using GPR and PAU, which were originally tuned for the detection of steel bars in traditional reinforced concrete elements. The detectability of the FRP bars embedded in concrete can be further verified by the use of advanced post processing algorithms such as SAFT (synthetic aperture focusing technique) or FMC/TFM (full matrix capture/total focusing method) in a follow up future study. Similarly, this study is limited to only three specimens with limited variation in depth of bars up to 3 in., which can be overcome in future studies by either conducting experimental verification on several specimens or by conducting numerical simulation analysis with adequate test parameters to collect more data for a statistically sound validation.

Author Contributions: Conceptualization, P.M., S.S.K.D. and A.B.M.; methodology, P.M., S.S.K.D. and J.D.O.; software, P.M., S.S.K.D. and K.D.; validation, A.B.M., A.N. and K.D.; formal analysis, A.B.M. and A.N.; investigation, P.M., S.S.K.D. and K.D.; resources, A.B.M., A.N. and K.D.; data curation, P.M., S.S.K.D. and J.D.O.; writing—original draft preparation, P.M.; writing—review and editing, A.B.M., A.N., S.S.K.D. and J.D.O.; visualization, P.M., S.S.K.D. and J.D.O.; supervision, A.B.M. and A.N.; project administration, A.B.M. and A.N.; funding acquisition, A.B.M. and A.N. All authors have read and agreed to the published version of the manuscript.

Funding: This research received no external funding.

Institutional Review Board Statement: Not applicable.

Informed Consent Statement: Not applicable.

Data Availability Statement: The data presented in this study are available by request from the corresponding author.

Acknowledgments: The authors greatly acknowledge the support by the Department of Civil and Environmental Engineering at Florida International University, the Department of Civil and Architectural Engineering at the University of Miami, especially Ana De Diego Castro, and Screening Eagle Technologies, Switzerland. The contents of this paper reflect the views of the authors, who are responsible for the facts and the accuracy of the information presented herein.

Conflicts of Interest: The authors declare no conflict of interest.

References

1. Wang, W. *Durability Behavior of Fiber Reinforced Polymer and Steel Reinforced Polymer for Infrastructure Applications*; Missouri University of Science and Technology: Rolla, MO, USA, 2017.
2. Benmokrane, B.; El-Salakawy, E.; El-Ragaby, A.; Lackey, T. Designing and Testing of a Concrete Bridge Deck Reinforced with Glass FRP Bars. *J. Bridg. Eng.* **2006**, *11*, 217–229. [CrossRef]
3. Khedmatgozar Dolati, S.S.; Mehrabi, A. NSM FRP Pile-Splice System for Prestressed Precast Concrete Piles. *Pract. Period. Struct. Des. Constr.* **2022**, *27*, 4022046. [CrossRef]
4. Dolati, S.S.K.; Mehrabi, A. FRP Sheet/Jacket System as an Alternative Method for Splicing Prestressed-Precast Concrete Piles. *Case Stud. Constr. Mater.* **2022**, *16*, e00912.
5. Mehrabi, A.; Khedmatgozar Dolati, S.S. NSMB Pile Splice System for Precast Concrete Piles. U.S. Patent 11,319,689, 3 May 2022.
6. Khedmatgozar Dolati, S.S.; Mehrabi, A. FRP Splice System for Joining Structural Elements. U.S. Patent 11,319,706, 3 May 2022.
7. Mohamed, H.M.; Benmokrane, B. Design and Performance of Reinforced Concrete Water Chlorination Tank Totally Reinforced with GFRP Bars: Case Study. *J. Compos. Constr.* **2014**, *18*, 1–11. [CrossRef]
8. Benmokrane, B.; Mohamed, H.M.; Mousa, S.; Elsafty, A.; Nolan, S. Design, Construction, Testing, and Behavior of Driven Precast Concrete Piles Reinforced with GFRP Bars and Spirals. *J. Bridg. Eng.* **2021**, *26*, 1–13. [CrossRef]
9. Yazdani, N.; Garcia, E.C.; Riad, M. *Field Assessment of Concrete Structures Rehabilitated with FRP*; Elsevier Ltd.: Amsterdam, The Netherlands, 2018; ISBN 9780081021811.
10. Dolati, S.S.K.; Matamoros, A.; Ghannoum, W. Evaluating the Effects of Loading Protocol on the Strength and Deformation Capacity of Flexure-Shear Critical Concrete Columns. *Eng. Struct.* **2023**, *279*, 115592. [CrossRef]
11. Javed, A.; Krishna, C.; Ali, K.; Afzal, M.F.U.D.; Mehrabi, A.; Meguro, K. Micro-Scale Experimental Approach for the Seismic Performance Evaluation of RC Frames with Improper Lap Splices. *Infrastructures* **2023**, *8*, 56. [CrossRef]
12. Malnati, P. A Hidden Revolution: FRP Rebar Gains New Strength. *Compos. Technol.* **2011**, *17*, 6.
13. Mirmiran, A.; Wei, Y. Damage Assessment of FRP-Encased Concrete Using Ultrasonic Pulse Velocity. *J. Eng. Mech.* **2001**, *127*, 126–135. [CrossRef]
14. Ghaib, M. Detection and Localization of Damage in Fiber Reinforced Polymer Bars Using Acoustic Emission, Micro Computed Tomography, and Scanning Electron Microscopy Techniques. Ph.D. Thesis, University of Manitoba, Winnipeg, MB, Canada, 2018.
15. Telang, N.M.; Dumlao, C.; Mehrabi, A.B.; Ciolko, A.T.; Gutierrez, J. NCHRP Report 564: Field Inspection of In-Service FRP Bridge Decks. *Transp. Res. Board* **2006**, *564*, 175. [CrossRef]
16. Khedmatgozar Dolati, S.S.; Malla, P.; Ortiz, J.D.; Mehrabi, A.; Nanni, A. Non-Destructive Testing Applications for in-Service FRP Reinforced/Strengthened Concrete Bridge Elements. In *Nondestructive Characterization and Monitoring of Advanced Materials, Aerospace, Civil Infrastructure, and Transportation XVI*; SPIE: Bellingham, WA, USA, 2022; Volume 12047, pp. 59–74.
17. Ortiz, J.D.; Khedmatgozar Dolati, S.S.; Malla, P.; Nanni, A.; Mehrabi, A. FRP-Reinforced/Strengthened Concrete: State-of-the-Art Review on Durability and Mechanical Effects. *Materials* **2023**, *16*, 1990. [CrossRef]
18. Kim, Y.J. *Use of Fiber-Reinforced Polymers in Highway Infrastructure*; National Academics: Washington, DC, USA, 2017; ISBN 9780309390040.
19. Karbhari, V.M.; Chin, J.W.; Hunston, D.; Benmokrane, B.; Juska, T.; Morgan, R.; Lesko, J.J.; Sorathia, U.; Reynaud, D. Durability Gap Analysis for Fiber-Reinforced Polymer Composites in Civil Infrastructure. *J. Compos. Constr.* **2003**, *7*, 238–247. [CrossRef]
20. Mohammedameen, A.; Gülşan, M.E.; Alzeebaree, R.; Çevik, A.; Niş, A. Mechanical and Durability Performance of FRP Confined and Unconfined Strain Hardening Cementitious Composites Exposed to Sulfate Attack. *Constr. Build. Mater.* **2019**, *207*, 158–173. [CrossRef]
21. Benmokrane, B.; El-Salakawy, E.; El-Ragaby, A.; El-Gamal, S. Performance Evaluation of Innovative Concrete Bridge Deck Slabs Reinforced with Fibre-Reinforced-Polymer Bars. *Can. J. Civ. Eng.* **2007**, *34*, 298–310. [CrossRef]
22. Ettouney, S.; Alampalli, M. *Infrastructure Health in Civil Engineering*; National Academics: Washington, DC, USA, 2011; ISBN 9781439866542.
23. Khanal, S. *Review of Modern Nondestructive Testing Techniques for Civil Infrastructure*; West Virginia University: Morgantown, WV, USA, 2020.

24. Wheeler, A.S. *Nondestructive Evaluation of Concrete Bridge Columns Rehabilitiated with Fiber Reinforced Polymers Using Digital Tap Hammer and Infrared Thermography Nondestructive Evaluation of Concrete Bridge Columns*; West Virginia University: Morgantown, WV, USA, 2018.
25. Halabe, U.B.; Joshi, R.M.; Gangarao, H.V.S. Nondestructive Testing of FRP Composite Structural Components and FRP Rehabilitated Bridge Using Digital Tap Testing. *J. Multidiscip. Eng. Sci. Technol.* **2020**, *7*, 11477–11482.
26. Taillade, F.; Quiertant, M.; Benzarti, K.; Dumoulin, J.; Aubagnac, C. Nondestructive Evaluation of FRP Strengthening Systems Bonded on RC Structures Using Pulsed Stimulated Infrared Thermography. In *Infrared Thermography*; IntechOpen: London, UK, 2012; Chapter 9; pp. 193–208.
27. Ekenel, M.; Myers, J.J. Nondestructive Evaluation of RC Structures Strengthened with FRP Laminates Containing Near-Surface Defects in the Form of Delaminations. *Sci. Eng. Compos. Mater.* **2007**, *14*, 299–315. [CrossRef]
28. Hsieh, C.T.; Lin, Y. Detecting Debonding Flaws at the Epoxy-Concrete Interfaces in near-Surface Mounted CFRP Strengthening Beams Using the Impact-Echo Method. *NDT E Int.* **2016**, *83*, 1–13. [CrossRef]
29. Crawford, K.C. Non-Destructive Testing of FRP-Structural Systems Applied to Concrete Bridges. In *Nondestructive Testing of Materials and Structures*; Springer: Dordrecht, The Netherlands, 2013; pp. 835–840.
30. Crawford, K.C. NDT Evaluation of Long-Term Bond Durability of CFRP-Structural Systems Applied to RC Highway Bridges. *Int. J. Adv. Struct. Eng.* **2016**, *8*, 161–168. [CrossRef]
31. *ACI Committee 228*; ACI 228.2R-13: Report on Nondestructive Test Methods for Evaluation of Concrete in Structures. ACI: Farmington Hills, MI, USA, 2013.
32. Dong, Y.; Ansari, F. Non-Destructive Testing and Evaluation (NDT/NDE) of Civil Structures Rehabilitated Using Fiber Reinforced Polymer (FRP) Composites. *Serv. Life Estim. Ext. Civ. Eng. Struct.* **2011**, *1*, 193–222. [CrossRef]
33. Gower, M.; Lodeiro, M.; Aktas, A.; Shaw, R.; Maierhofer, C.; Krankenhagen, R.; Augustin, S.; Rollig, M.; Knazovicka, L.; Blahut, A.; et al. Design and Manufacture of Reference and Natural Defect Artefacts for the Evaluation of NDE Techniques for Fibre Reinforced Plastic (FRP) Composites in Energy Applications. In Proceedings of the 19th World Conference on Non-Destructive Testing, Munich, Germany, 13–17 June 2016.
34. Aboukhousa, M.; Qaddoumi, N. Near-Field Microwave Imaging of Subsurface Inclusions in Laminated Composite Structures. In Proceedings of the 16th World Conference on Nondestructive Testing, Montreal, QC, Canada, 30 August–3 September 2004.
35. Kharkovsky, S.; Ryley, A.C.; Stephen, V.; Zoughi, R. Dual-Polarized near-Field Microwave Reflectometer for Noninvasive Inspection of Carbon Fiber Reinforced Polymer-Strengthened Structures. *IEEE Trans. Instrum. Meas.* **2008**, *57*, 168–175. [CrossRef]
36. Navagato, M.D.; Narayanan, R.M. Microwave Imaging of Multilayered Structures Using Ultrawideband Noise Signals. *NDT E Int.* **2019**, *104*, 19–33. [CrossRef]
37. Ekenel, M.; Stephen, V.; Myers, J.J.; Zoughi, R. Microwave NDE of Reinforced Concrete Beams Strengthened with CFRP Laminates Containing Surface Defects and Tested under Cyclic Loading. In Proceedings of the 16th World Conference on Nondestructive Testing, Montreal, QC, Canada, 30 August–3 September 2004.
38. Akuthota, B.; Hughes, D.; Zoughi, R.; Myers, J.; Nanni, A. Near-Field Microwave Detection of Disbond in Carbon Fiber Reinforced Polymer Composites Used for Strengthening Cement-Based Structures and Disbond Repair Verification. *J. Mater. Civ. Eng.* **2004**, *16*, 540–546. [CrossRef]
39. Dutta, S.S. Nondestructive Evaluation of FRP Wrapped Concrete Cylinders Using Infrared Thermography and Groud Penetrating Radar. Master of Science Thesis, West Virginia University, Morgantown, WV, USA, 2006.
40. Jackson, D.; Islam, M.; Alampalli, S. Feasibility of Evaluating the Performance of Fiber Reinforced Plastic (FRP) Wrapped Reinforced Concrete Columns Using Ground Penetrating RADAR (GPR) and Infrared (IR) Thermography Techniques. In *Structural Materials Technology IV—An NDT Conference*; CRC Press: Boca Raton, FL, USA, 2000; pp. 390–395.
41. Hing, C.L.C.; Halabe, U.B. Nondestructive Testing of GFRP Bridge Decks Using Ground Penetrating Radar and Infrared Thermography. *J. Bridg. Eng.* **2010**, *15*, 391–398. [CrossRef]
42. Yazdani, N.; Beneberu, E.; Riad, M. Nondestructive Evaluation of FRP-Concrete Interface Bond Due to Surface Defects. *Adv. Civ. Eng.* **2019**, *2019*, 2563079. [CrossRef]
43. Büyüköztürk, O.; Yu, T.Y. Far-Field Radar NDT Technique for Detecting GFRP Debonding from Concrete. *Constr. Build. Mater.* **2009**, *23*, 1678–1689. [CrossRef]
44. Sen, R. Developments in the Durability of FRP-Concrete Bond. *Constr. Build. Mater.* **2015**, *78*, 112–125. [CrossRef]
45. Riad, M.; Yazdani, N.; Almomani, Y.; Gonzalez, E. Utilization of Ground Penetrating Radar (GPR) in the Non-Destructive Assessment of FRP Laminate-Concrete Bond Strength. In *Advances and Challenges in Structural Engineering, Proceedings of the International Congress and Exhibition "Sustainable Civil Infrastructures", Cairo, Egypt, 10–19 November 2019*; Springer Science and Business Media: Berlin, Germany, 2019; pp. 244–267.
46. Jaishankar, P.; Kanchidurai, S.; Thomas, A.C.; Mohan, K.S.R. Experimental Investigation on Non-Destructive Behaviour of Repaired FRP Concrete Beams. *Mater. Today Proc.* **2022**, *64*, 990–994. [CrossRef]
47. Liu, Z.; Gu, X.; Chen, J.; Wang, D.; Chen, Y.; Wang, L. Automatic Recognition of Pavement Cracks from Combined GPR B-Scan and C-Scan Images Using Multiscale Feature Fusion Deep Neural Networks. *Autom. Constr.* **2023**, *146*, 104698. [CrossRef]
48. La Malfa Ribolla, E.; Hajidehi, M.R.; Rizzo, P.; Scimemi, G.F.; Spada, A.; Giambanco, G. Ultrasonic Inspection for the Detection of Debonding in CFRP-Reinforced Concrete. *Struct. Infrastruct. Eng.* **2017**, *14*, 807–816. [CrossRef]

49. Concu, G.; Trulli, N. Direct and Semi-Direct Ultrasonic Testing for Quality Control of FRC-Concrete Adhesion. *Structures* **2021**, *32*, 54–64. [CrossRef]
50. Gunes, O. Failure Modes in Structural Applications of Fiber-Reinforced Polymer (FRP) Composites and Their Prevention. In *Developments in Fiber-Reinforced Polymer (FRP) Composites for Civil Engineering*; Woodhead Publishing Series in Civil and Structural Engineering; Woodhead Publishing: Sawston, UK, 2013; ISBN 9781845691455.
51. Ribolla, E.L.M.; Hajidehi, M.R.; Scimemi, G.F.; Spada, A.; Giambanco, G. Assessment of Bonding Defects in FRP Reinforced Structures via Ultrasonic Technique. *Chall. J. Struct. Mech.* **2016**, *2*, 3. [CrossRef]
52. Ray, B.C.; Hasan, S.T.; Clegg, D.W. Evaluation of Defects in FRP Composites by NDT Techniques. *J. Reinf. Plast. Compos.* **2007**, *26*, 1187–1192. [CrossRef]
53. Taheri, H.; Hassen, A.A. Nondestructive Ultrasonic Inspection of Composite Materials: A Comparative Advantage of Phased Array Ultrasonic. *Appl. Sci.* **2019**, *9*, 1628. [CrossRef]
54. Boychuk, A.S.; Generalov, A.S.; Stepanov, A.V. Nondestructive Testing of FRP by Using Phased Array Ultrasonic Technology. In Proceedings of the ICNDT 2013: 12th International NDT Conference—Application of Contemporary Non-Destructive Testing in Engineering, Portorož, Slovenia, 4–6 September 2013; pp. 51–55.
55. Meola, C.; Boccardi, S.; Carlomagno, G.M.; Boffa, N.D.; Monaco, E.; Ricci, F. Nondestructive Evaluation of Carbon Fibre Reinforced Composites with Infrared Thermography and Ultrasonics. *Compos. Struct.* **2015**, *134*, 845–853. [CrossRef]
56. Wen, B.; Zhou, Z.; Zeng, B.; Yang, C.; Fang, D.; Xu, Q.; Shao, Y.; Wan, C. Pulse-Heating Infrared Thermography Inspection of Bonding Defects on Carbon Fiber Reinforced Polymer Composites. *Sci. Prog.* **2020**, *103*, 36850420950131. [CrossRef]
57. Caldeira, M.M.; Padaratz, I.J. Potentialities of Infrared Thermography to Assess Damage in Bonding between Concrete and GFRP. *Rev. IBRACON Estrut. Mater.* **2015**, *8*, 296–322. [CrossRef]
58. Brown, J.R.; Chittineni, S.H. Comparison of Lock-in and Pulse-Phase Thermography for Defect Characterization in FRP Composites Applied to Concrete. *Therm. Infrared Appl. XXXVII* **2015**, *9485*, 94850B. [CrossRef]
59. Milovanović, B.; Banjad Pečur, I. Review of Active IR Thermography for Detection and Characterization of Defects in Reinforced Concrete. *J. Imaging* **2016**, *2*, 11. [CrossRef]
60. Riad, M. Quantitative Non-Destructive Evaluation (NDE) of FRP Laminate-Concrete Bond Strength. Ph.D. Thesis, The University of Texas at Arlington, Arlington, TX, USA, 2017.
61. Tashan, J.; Al-Mahaidi, R.; Mamkak, A. Defect Size Measurement and Far Distance Infrared Detection in CFRP-Concrete and CFRP-Steel Systems. *Aust. J. Struct. Eng.* **2016**, *17*, 2–13. [CrossRef]
62. Mabry, N.J.; Peters, K.J.; Seracino, R. Depth Detection of Bond Defects in Multilayered Externally Bonded CFRP-to-Concrete Using Pulse Phase Thermography. *J. Compos. Constr.* **2015**, *19*, 04015002. [CrossRef]
63. Gu, J.C.; Unjoh, S.; Naito, H. Detectability of Delamination Regions Using Infrared Thermography in Concrete Members Strengthened by CFRP Jacketing. *Compos. Struct.* **2020**, *245*, 112328. [CrossRef]
64. Yumnam, M.; Gupta, H.; Ghosh, D.; Jaganathan, J. Inspection of Concrete Structures Externally Reinforced with FRP Composites Using Active Infrared Thermography: A Review. *Constr. Build. Mater.* **2021**, *310*, 125265. [CrossRef]
65. Wang, B.; Zhong, S.; Lee, T.-L.; Fancey, K.S.; Mi, J. Non-Destructive Testing and Evaluation of Composite Materials/Structures: A State-of-the-Art Review. *Adv. Mech. Eng.* **2020**, *12*, 1687814020913761. [CrossRef]
66. Carpinteri, A.; Lacidogna, G.; Paggi, M. Acoustic Emission Monitoring and Numerical Modeling of FRP Delamination in RC Beams with Non-Rectangular Cross-Section. *Mater. Struct. Constr.* **2007**, *40*, 553–566. [CrossRef]
67. Degala, S.; Rizzo, P.; Ramanathan, K.; Harries, K.A. Acoustic Emission Monitoring of CFRP Reinforced Concrete Slabs. *Constr. Build. Mater.* **2009**, *23*, 2016–2026. [CrossRef]
68. Saeedifar, M.; Fotouhi, M.; Ahmadi Najafabadi, M.; Hosseini Toudeshky, H.; Minak, G. Prediction of Quasi-Static Delamination Onset and Growth in Laminated Composites by Acoustic Emission. *Compos. Part B Eng.* **2016**, *85*, 113–122. [CrossRef]
69. Taillade, F.; Quiertant, M.; Benzarti, K.; Aubagnac, C.; Moser, E. Non-Destructive Evaluation (NDE) of Composites: Using Shearography to Detect Bond Defects. In *Non-Destructive Evaluation (NDE) of Polymer Matrix Composites*; Woodhead Publishing Series in Composites Science and Engineering; Woodhead Publishing: Sawston, UK, 2013; pp. 542–556. [CrossRef]
70. Yu, T.; Cheng, T.K.; Zhou, A.; Lau, D. Remote Defect Detection of FRP-Bonded Concrete System Using Acoustic-Laser and Imaging Radar Techniques. *Constr. Build. Mater.* **2016**, *109*, 146–155. [CrossRef]
71. Qiu, Q.; Lau, D. Defect Detection of FRP-Bonded Civil Structures under Vehicle-Induced Airborne Noise. *Mech. Syst. Signal Process.* **2021**, *146*, 106992. [CrossRef]
72. Qiu, Q.; Lau, D. A Novel Approach for Near-Surface Defect Detection in FRP-Bonded Concrete Systems Using Laser Reflection and Acoustic-Laser Techniques. *Constr. Build. Mater.* **2017**, *141*, 553–564. [CrossRef]
73. Qiu, Q.; Lau, D. Experimental Evaluation on the Effectiveness of Acoustic-Laser Technique towards the FRP-Bonded Concrete System. In *Structural Health Monitoring and Inspection of Advanced Materials, Aerospace, and Civil Infrastructure 2015, Proceedings of the SPIE Smart Structures and Materials + Nondestructive Evaluation and Health Monitoring, San Diego, CA, USA, 8–12 March 2015*; SPIE: San Diego, CA, USA; Volume 9437, p. 943705. [CrossRef]
74. Yang, L. Recent Developments in Digital Shearography for Nondestructive Testing. *Mater. Eval.* **2006**, *64*, 704–709.
75. Choi, S.W.; Lee, J.H. Nondestructive Evaluation of Internal Defects for Composite Materials by Using Shearography. *Key Eng. Mater.* **2004**, *270–273*, 781–786. [CrossRef]

76. Wan, B. *Using Fiber-Reinforced Polymer (FRP) Composites in Bridge Construction and Monitoring Their Performance: An Overview*; Woodhead Publishing: Sawston, UK, 2014; ISBN 9780857097019.
77. Garney, G. *Defects Found Through Non-Destructive Testing Methods of Fiber Reinforced Polymeric Composites*; California State University: Fullerton, CA, USA; Ann Arbor, MI, USA, 2006.
78. Weissenböck, J.; Reh, A.; Salaberger, D.; Heinzl, C.; Kastner, J. Advanced Visualization and Exploration Techniques for Fiber Reinforced Polymers. In Proceedings of the 11th European Conference on Non-Destructive Testing (ECNDT 2014), Prague, Czech Republic, 6–11 October 2014; pp. 1–10.
79. Rodríguez-Hortalá, M.; Hatzmann, J.; Degischer, H.P. Structural Characterisation of Defects in CFRP Laminates Produced with Different Epoxy Resin Systems and Their Influence on the Mechanical Properties. In Proceedings of the ECCM 2012—Composites at Venice, 15th European Conference on Composite Materials, Tarrytown, NY, USA, 6–8 June 2012; pp. 24–28.
80. Khosravani, M.R.; Reinicke, T. On the Use of X-Ray Computed Tomography in Assessment of 3D-Printed Components. *J. Nondestruct. Eval.* **2020**, *39*, 75. [CrossRef]
81. Kim, S.Y.; Sesso, M.L.; Franks, G.V. In-Situ 4-Point Flexural Testing and Synchrotron Micro X-Ray Computed Tomography of 3D Printed Hierarchical-Porous Ultra-High Temperature Ceramic. *Addit. Manuf.* **2022**, *54*, 102728. [CrossRef]
82. Karbhari, V.M.; Kaiser, H.; Navada, R.; Ghosh, K.; Lee, L. *Methods for Detecting Defects in Composite Rehabilitated Concrete Structures*; Oregon Department of Transportation: Salem, OR, USA; Federal Highway Administration: Washington, DC, USA, 2005.
83. Alampalli, S. Field Performance of an FRP Slab Bridge. *Compos. Struct.* **2006**, *72*, 494–502. [CrossRef]
84. Guan, H.; Karbhari, V.M.; Sikorsky, C.S. Long-Term Structural Health Monitoring System for a FRP Composite Highway Bridge Structure. *J. Intell. Mater. Syst. Struct.* **2007**, *18*, 809–823. [CrossRef]
85. Hag-elsafi, O.; Kunin, J.; Alampalli, S.; Conway, T. *Strengthening of Route 378 Bridge Over Wynantskill Creek In New York Using FRP Laminates*; National Academies of Sciences, Engineering, and Medicine: Washington, DC, USA, 2001.
86. Hag-elsafi, O.; Lund, R.; Alampalli, S. *Strengthening of Church Street Bridge Pier Capbeam Using Bonded FRP Composite Plates: Strengthening and Load Testing*; Transportation Research and Development Bureau: New York, NY, USA, 2002.
87. Afzal, M.F.U.D.; Matsumoto, Y.; Nohmi, H.; Sakai, S.; Su, D.; Nagayama, T. Comparison of Radar Based Displacement Measurement Systems with Conventional Systems in Vibration Measurements at a Cable Stayed Bridge. In Proceedings of the 11th German-Japan Bridge Symposium, Osaka, Japan, 30–31 August 2016.
88. Li, W.; Ho, S.C.M.; Patil, D.; Song, G. Acoustic Emission Monitoring and Finite Element Analysis of Debonding in Fiber-Reinforced Polymer Rebar Reinforced Concrete. *Struct. Health Monit.* **2017**, *16*, 674–681. [CrossRef]
89. Xu, K.; Ren, C.; Deng, Q.; Jin, Q.; Chen, X. Real-Time Monitoring of Bond Slip between GFRP Bar and Concrete Structure Using Piezoceramic Transducer-Enabled Active Sensing. *Sensors* **2018**, *18*, 2653. [CrossRef]
90. Sharma, G.; Sharma, S.; Sharma, S.K. Fracture Monitoring of Steel and GFRP Reinforced Concrete Beams Using Acoustic Emission and Digital Image Correlation Techniques. *Struct. Concr.* **2021**, *22*, 1962–1976. [CrossRef]
91. Dolati, S.S.K.; Mehrabi, A.; Dolati, S.S.K.; Caluk, N. NDT Methods for Damage Detection in Steel Bridges. *Proc. SPIE* **2022**, *12048*, 385–394.
92. Khedmatgozar Dolati, S.S.; Caluk, N.; Mehrabi, A.; Khedmatgozar Dolati, S.S. Non-Destructive Testing Applications for Steel Bridges. *Appl. Sci.* **2021**, *11*, 9757. [CrossRef]
93. Drobiec, Ł.; Jasiński, R.; Mazur, W. The Use of Non-Destructive Methods to Detect Non-Metallic Reinforcement in Concrete and Masonry. *Preprints* **2019**, 2019010021, *Preprints*. [CrossRef]
94. *ASTM C39*; Standard Test Method for Compressive Strength of Cylindrical Concrete Specimens. ASTM: West Conshohocken, PA, USA, 2010.
95. Hameed, A.; Rasool, A.M.; Ibrahim, Y.E.; Afzal, M.F.U.D.; Qazi, A.U.; Hameed, I. Utilization of Fly Ash as a Viscosity-Modifying Agent to Produce Cost-Effective, Self-Compacting Concrete: A Sustainable Solution. *Sustainability* **2022**, *14*, 1559. [CrossRef]
96. *ACI CODE-440.11-22*; Building Code Requirements for Structural Concrete Reinforced with Glass Fiber-Reinforced Polymer (GFRP) Bars—Code and Commentary. ACI: Farmington Hills, MI, USA, 2022.
97. Javed, A.; Sadeghnejad, A.; Rehmat, S.; Yakel, A.; Azizinamini, A. *Magnetic Flux Leakage Method for Damage Detection in Internal Post-Tensioning Tendons*; Florida Department of Transportation: Tallahassee, FL, USA, 2021; 166p.
98. Tosti, F.; Ferrante, C. *Using Ground Penetrating Radar Methods to Investigate Reinforced Concrete Structures*; Springer: Dordrecht, The Netherlands, 2020; Volume 41, ISBN 0123456789.
99. Liu, Z.; Yeoh, J.K.W.; Gu, X.; Dong, Q.; Chen, Y.; Wu, W.; Wang, L.; Wang, D. Automatic Pixel-Level Detection of Vertical Cracks in Asphalt Pavement Based on GPR Investigation and Improved Mask R-CNN. *Autom. Constr.* **2023**, *146*, 104689. [CrossRef]
100. Capozzoli, L.; Rizzo, E. Combined NDT Techniques in Civil Engineering Applications: Laboratory and Real Test. *Constr. Build. Mater.* **2017**, *154*, 1139–1150. [CrossRef]
101. Sensors and Software. *Conquest 100 User's Guide*; Sensors and Software: Mississauga, ON, Canada, 2015.
102. IDS Georadar. *C-Thrue User Manual: All-in-One Ground Penetrating Radar (GPR) for Non-Destructive Testing of Concrete Structures User*; IDS Georadar: Pisa, Italy, 2017.
103. Screening Eagle. *Sales Flyer: Proceq Ground Penetrating Radars GP8000*; Screening Eagle: Austin, TX, USA, 2022.
104. Screening Eagle. *Sales Flyer: Proceq Ground Penetrating Radars GP8800*; Screening Eagle: Austin, TX, USA, 2022.
105. Chen, R.; Tran, K.T.; Dinh, K.; Ferraro, C.C. Evaluation of Ultrasonic SH-Waveform Tomography for Determining Cover Thickness and Rebar Size in Concrete Structures. *J. Nondestruct. Eval.* **2022**, *41*, 1–16. [CrossRef]

106. Torres-González, M.; Mantero, J.; Hurtado, S.; Flores-Alés, V.; Alejandre, F.J.; Alducín-Ochoa, J.M. Characterization and Radioactive Evaluation of the Concrete from a Radiotherapy Bunker. *Struct. Concr.* **2022**, *23*, 3102–3113. [CrossRef]
107. Park, S.; Kim, J.; Jeon, K.; Kim, J.; Park, S. Improvement of Gpr-Based Rebar Diameter Estimation Using Yolo-V3. *Remote Sens.* **2021**, *13*, 2011. [CrossRef]
108. Shull, P.J. *Nondestructive Evaluation Theory, Techniques, and Applications*; Marcel Dekker, Inc.: New York, NY, USA, 2001; ISBN 0824788729.
109. Boychuk, A.S.; Generalov, A.S.; Stepanov, A.V. CFRP Structural Health Monitoring by Ultrasonic Phased Array Technique. In Proceedings of the 7th European Workshop on Structural Health Monitoring. EWSHM 2014—2nd European Conference of the Prognostics and Health Management Society, Nantes, France, 8–11 July 2014; pp. 2206–2211.
110. Ryan, T.W.; EricMann, J.; Chill, Z.M.; Ott, B.T. Bridge Inspector's Reference Manual. *Fhwa* **2012**, *BIRM 1*, 1020.
111. Taheri, H.; Delfanian, F.; Du, J. Acoustic Emission and Ultrasound Phased Array Technique For Composite Material Evaluation. In Proceedings of the ASME 2013 International Mechanical Engineering Congress and Exposition, San Diego, CA, USA, 15–21 November 2013; pp. 1–8.
112. Prabhakara, P.; Mielentz, F.; Stolpe, H.; Behrens, M.; Lay, V.; Niederleithinger, E. Validation of Novel Ultrasonic Phased Array Borehole Probe by Using Simulation and Measurement. *Sensors* **2022**, *22*, 9823. [CrossRef]
113. Screening Eagle. *Sales Flyer: Pundit Live Array Pro Pulse Echo Testing with A.I.*; Screening Eagle: Austin, TX, USA, 2018.
114. Acoustic Control Systems. *Product Flyer: A1040 MIRA 3D*; Acoustic Control Systems: North Yorkshire, UK, 2022.
115. Dinh, K.; Tran, K.; Gucunski, N.; Ferraro, C.C.; Nguyen, T. Imaging Concrete Structures with Ultrasonic Shear Waves—Technology Development and Demonstration of Capabilities. *Infrastructures* **2023**, *8*, 53. [CrossRef]
116. Annan, A.P. Ground Penetrating Radar Principles, Procedures & Applications. In *Ground Penetrating Radar Theory and Application*; Elsevier Science: Amsterdam, The Netherlands, 2009; p. iv. [CrossRef]
117. Gehrig, M.D.; Morris, D.V.; Bryant, J.T. Ground Penetrating Radar for Concrete Evaluation Studies. In Proceedings of the Foundation Performance Association Meeting, London, UK, 24 March 2004; pp. 1–17.
118. Tsalicoglou, I. The Three (Four) Musketeers of Multi-Technology Concrete NDT for Accuracy and Productivity. In Proceedings of the 3rd Japanese-Swiss Workshop—"Durability Testing of Concrete, on Site and in the Lab", Wildegg, Switzerland, 16 October 2018.

Disclaimer/Publisher's Note: The statements, opinions and data contained in all publications are solely those of the individual author(s) and contributor(s) and not of MDPI and/or the editor(s). MDPI and/or the editor(s) disclaim responsibility for any injury to people or property resulting from any ideas, methods, instructions or products referred to in the content.